

Visualization by scanning SQUID microscopy of the intermediate state in the superconducting Dirac semimetal PdTe₂

P. Garcia-Campos,^{1,*} Y. K. Huang,² A. de Visser,² and K. Hasselbach^{1,†}

¹*Université Grenoble Alpes & Institut Néel, CNRS, 38042 Grenoble, France*

²*Van der Waals-Zeeman Institute, University of Amsterdam, Science Park 904, 1098 XH Amsterdam, Netherlands*

(Dated: March 13, 2022)

The Dirac semimetal PdTe₂ becomes superconducting at a temperature $T_c = 1.6$ K. Thermodynamic and muon spin rotation experiments support type-I superconductivity, which is unusual for a binary compound. A key property of a type-I superconductor is the intermediate state which presents a coexistence of superconducting and normal domains (flux structures) at magnetic fields lower than the thermodynamic critical field H_c . By means of scanning SQUID microscopy (SSM) we observe flux structures in the superconducting state of PdTe₂. The flux structures are strongly history dependent with a transition from round shapes to laminar shapes as the magnetic field is more and more increased. The field amplitudes measured at the surface are indicative for the presence of Landau branching. The domain wall width in the intermediate state has been determined.

I. INTRODUCTION

Finding materials presenting topological superconductivity is an important challenge in today's condensed matter research. Topological superconductors are predicted to host Majorana zero modes at their surface, which could be used for quantum computation with increased coherence times because the surface states are protected by symmetry^{1,2}. A wide range of unconventional superconductors is under scrutiny for finding fingerprints of topologically protected states³⁻⁵. A promising family of materials are the transition metal dichalcogenides, to which PdTe₂ belongs. Angle resolved photoemission spectroscopy (ARPES) has identified PdTe₂ as a Dirac semimetal, with a tilted Dirac cone below the Fermi energy with spin-polarized topological surface states⁶⁻⁸. Since the tilt parameter $k > 1$ PdTe₂ is classified as a type-II Dirac semimetal⁹. PdTe₂ is also a superconductor below $T_c = 1.6$ K¹⁰, with a conventional fully-gapped order parameter indicated by the step in the specific heat at T_c , $\Delta C/\gamma T_c \approx 1.5$ ¹¹ (γ is the Sommerfeld coefficient), and supported by the exponential temperature variation of the London penetration depth^{12,13}. Scanning tunneling microscopy and spectroscopy (STM/STS)^{7,14,15} and point contact spectroscopy (PCS)¹⁶ measurements report a BCS gap size Δ_{BCS} of the order of 215–326 μ eV, which gives rise to $2\Delta_{BCS}/k_B T_c$ in the range 3.0–4.2, *i.e.* close to the weak coupling value of 3.52.

The superconducting state of PdTe₂ in applied magnetic fields is subject of debate. Dc-magnetization and ac-susceptibility measurements show the presence of the differential paramagnetic effect (DPE) in applied magnetic fields $(1 - N)H_c < H_a < H_c$, where $\mu_0 H_c = 13.6$ mT is the thermodynamic critical field¹⁷. N is the demagnetization factor of the single crystal used in the experiment. This provides strong evidence for the existence of the intermediate state, which presents a macroscopic phase separation in superconducting and normal domains and is a key property of a type-I su-

perconductor¹⁸. Type-I superconductivity is in-line with the reported value of the Ginzburg-Landau parameter $\kappa = \lambda/\xi \approx 0.09 - 0.34$ ^{12,17}, where λ is the magnetic penetration depth and ξ the superconducting coherence length. This value of κ is smaller than the theoretical boundary value $1/\sqrt{2}$, above which type-II behavior is expected. On the other hand, STM/STS^{14,15} and PCS¹⁶ experiments have given rise to an interpretation in terms of a mixed type-I and type-II superconducting phase along with a spatial distribution of critical fields. This was attributed to an intrinsic electronic inhomogeneity already present in the normal phase. In another STM/STS measurement⁷ the observation of a vortex core and type-II superconductivity is reported. However, in all these STM/STS experiments an Abrikosov vortex lattice, which is the hall mark of type-II superconductivity¹⁸, was not observed. More recently, transverse muon spin rotation (μ SR) measurements have been conducted to probe the intermediate phase on the microscopic scale¹⁹. The results provide solid evidence for type-I superconductivity in the bulk of the PdTe₂ crystal.

Another intriguing aspect is the observation of a pronounced diamagnetic screening signal in the ac-susceptibility for applied fields $H_a > H_c$ ¹⁷. This has been interpreted as an unusual form of surface superconductivity, possibly related to the topological surface states that were detected by ARPES^{6,20}. The screening signal at the surface is preserved under pressure, which indicates it is a robust feature²¹. Finally, electrical resistivity measurements reveal superconductivity up to fields of the order of 0.3 T^{17,22}, that are much higher than the thermodynamic critical field (13.6 mT) and the surface critical field (34.9 mT)¹⁷. In this respect, the $H-T$ phase diagram presents similarities with those of so-called type-II/1 superconductors with $\kappa \approx 1/\sqrt{2}$ ^{23,24}.

These puzzling results and their interpretation provide the motivation to study the magnetic flux structure in the superconducting phase at the local scale. Here we report local magnetization measurements in the super-

conducting phase of a PdTe₂ single crystal using a scanning SQUID microscope²⁵. The observed flux structures confirm the presence of the intermediate state. They show a strong history dependence and a transition from a closed round shape to an open laminar-like shape as the magnetic field is more and more increased.

II. EXPERIMENTAL METHODS

Our measurements were made with a high-resolution scanning μ -SQUID microscope (SSM) working in a dilution refrigerator^{25,26}. The microscope combines tuning fork based scanning force microscopy and magnetic microscopy using a μ -SQUID scanning parallel to the sample surface at a distance of 350 nm from the sample surface. The microscope is equipped with three piezoelectric motors for the coarse approach in the x , y and z directions. A large range scanner moves the sample as much as 85 μm in the x and y directions relative to the μ -SQUID tip. By means of the inverted dilution refrigerator the sample can be cooled down to temperatures as low as 0.2 K. The square shaped aluminum μ -SQUID has an effective area ($S_{SQUID} = 0.36 \mu\text{m}^2$), with Dayem bridges as weak links. These devices are hysteretic, and therefore cannot be used in a flux-locked loop. Instead the current through the μ -SQUID is ramped until the transition into the voltage state at the critical current, I_c , is detected and recorded. The critical current of the μ -SQUID is a periodic function of the flux, Φ , penetrating the SQUID loop, with a period equal to the magnetic flux quantum $\Phi_0 = h/2e$. By repeatedly measuring the critical current we achieve a flux resolution of $1.2 \times 10^{-4} \Phi_0/\sqrt{\text{Hz}}$.

The scanned images shown in this work represent maps of the magnetic field above the sample surface. The SQUID microscope acquires critical current maps as a function of the SQUID's position above the surface. The magnetic field is obtained thanks to the previous calibration of the I_c curve, acquired while the sample was in the normal state ($\mu_0 H = \Phi/S_{SQUID}$).

The measurements were performed on a PdTe₂ single crystal in the shape of a flat rectangular prism with a length 0.88 mm, width 0.84 mm and thickness 0.097 mm. We benefit from the fact that the crystal was already used for measurements of the London penetration depth, $\lambda(T)$, as crystal s1 in Ref. 12. The onset superconducting transition temperature was found to be 1.67 K and the zero temperature penetration depth $\lambda(0) = 377$ nm. Here the magnetic field was applied perpendicular to the flat surface, *i.e.* the c -axis in the trigonal CdI₂ structure²⁷. In between the measurements the sample was stored in a desiccator. In the SSM measurements the applied field is also directed along the c -axis. A demagnetization factor $N = 0.82$ is calculated in the completely shielded case (susceptibility $\chi = -1$)²⁸. We remark this value is reduced to ~ 0.78 in the paramagnetic normal phase²⁹.

III. RESULTS

In order to investigate the $H - T$ phase diagram we have analyzed the SQUID response by increasing the applied field, H_a , after zero field cooling (ZFC), at a number of fixed temperatures. In Fig. 1(a), we show the critical current, I_c , as a function of H_a for three different temperatures: $T = 1.7$ K (black line), 1 K (blue line) and 0.3 K (red line). At $T = 1.7$ K the sample is in the normal state and the data shows the modulation (arcs) of the SQUID's I_c . Each period corresponds to one flux quantum entering the SQUID loop. At 1 K and 0.3 K the sample is in the superconducting phase. The data starts off with a flat response, which corresponds to Meissner screening, up to a field $H_p = (1 - N)H_c$. There above flux penetrates, as indicated by the fluctuating signal, up to H_c , above which the non-affected arcs are recovered. The field values $(1 - N)H_c$ and H_c measured in this way are indicated by arrows in Fig. 1(a). In between these fields we denote a significant change in the SQUID response, from large to small fluctuations of I_c , at a *fusing* field, H_f . As we will show in the next section, at this field single magnetic structures start fusing into laminar structures.

In Fig. 1(b) we have collected $(1 - N)H_c$, H_f and H_c obtained at thirteen different temperatures. H_c follows the standard BCS behavior, $H_c(T) = H_c(0)[1 - (T/T_c)^2]$, with $\mu_0 H_c = 13.62 \pm 0.05$ mT and $T_c = 1.57 \pm 0.01$ K. These values are in excellent agreement with the $H_c(T)$ behavior reported in Ref. 17. Correspondingly, we obtain $\mu_0(1 - N)H_c(0) = 3.83 \pm 0.03$ mT which gives us a demagnetization factor $N = 0.72$. This value is smaller than the calculated one, $N = 0.82$, which we attribute to a measured effective value $N_{eff} < N$ due to the local probe geometry. The data confirms the presence of the intermediate state in the slab-shaped sample and type-I superconductivity in PdTe₂. The effectiveness of this method for determining the phase diagram is indicative of a very low resistance to flux penetration and weak flux pinning in PdTe₂.

A. PdTe₂ Zero Field Cooled

In order to investigate how the flux penetration develops in the intermediate phase, we imaged the crystal at $T = 0.9$ K for different applied fields after ZFC (see Fig. 2). At the lowest applied field $\mu_0 H_a = 1$ mT we expect flux exclusion, which is confirmed by the data in Fig. 2(a). Nonetheless, some magnetic structures are observed, but since they do not evolve with the applied magnetic field, we conclude they were created by the residual magnetic field when ZFC. The field profile of the smallest structure along line A is plotted in Fig. 2(e). For comparison, the theoretical field distribution in the London limit of a hypothetical vortex of $7\Phi_0$ with a penetration depth $\lambda_{eff} = 2.1 \mu\text{m}$ and scanned at a height of 350 nm above the surface is given by the red line³⁰.

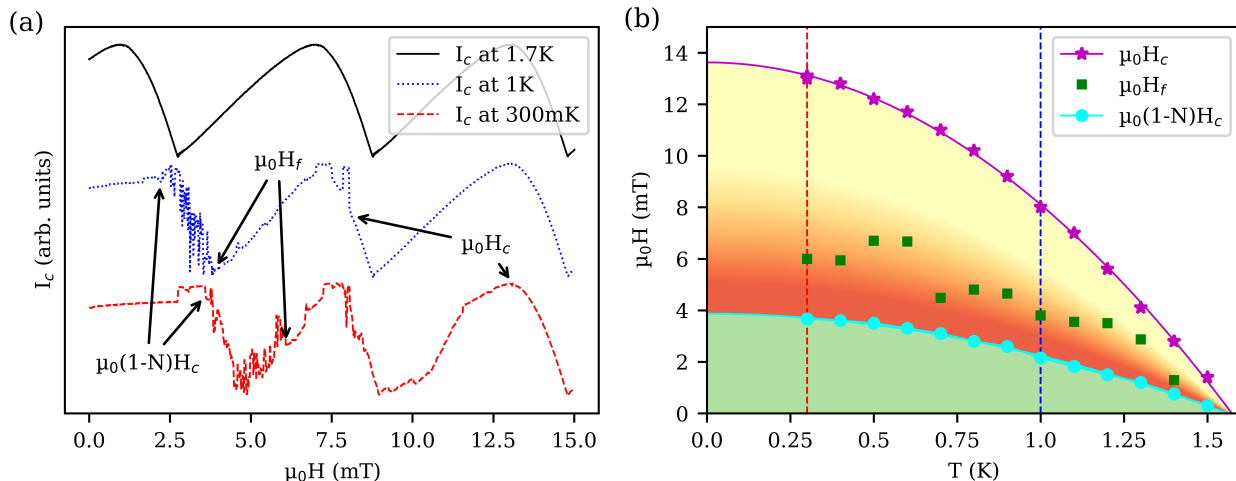


FIG. 1: (Color online) (a) The SQUID response after ZFC at three temperatures as indicated. In the normal phase (black solid line) the SQUID response is smooth. In the superconducting phase we distinguish three different behaviors: (i) flat signal, *i.e.* screening for $H < (1 - N)H_c$, (ii) high density of jumps, *i.e.* penetration of field in closed topology structures for $(1 - N)H_c < H < H_f$, and (iii) smoother jumps, *i.e.* open topology structures become more stable for $H_f < H < H_c$. The fields $H_p = (1 - N)H_c$, H_f and H_c are indicated by arrows. In (b) the phase diagram is constructed from the derived characteristic field values. The solid red line represents a BCS-fit $H_c(T) = H_c(0)[1 - (T/T_c)^2]$ with $\mu_0 H_c(0) = 13.62$ mT and $T_c = 1.57$ K and the solid blue line the equivalent fit with $\mu_0 H_p(0) = 3.83$ mT and $T_c = 1.58$ K. The vertical dashed lines indicate the temperatures at which the SQUID response is shown in (a).

The large λ_{eff} compared to the λ obtained by Salis *et al.*¹² ($\lambda \sim 377$ nm) could be indicative for a more important field spreading effect upon approaching the surface than in type-II superconductors. We remark that this structure is the least intense we found.

When H_p is crossed, magnetic structures fill the space, as demonstrated by the scans at 3.5, 4.5 and 7.5 mT (Fig. 2). At 3.5 mT (see Fig. 2(b)) the structures have a closed topology and they form a lattice, a self-organized structure reported frequently³¹. We notice two types of magnetic structures with closed topology: *mountains*, see the structures in Fig. 2(a) and the profile in Fig. 2(e), and *volcanoes*, see Fig. 2(b) and the profile in Fig. 2(f). A typical *volcano* structure, obtained by the field profile taken along line B in Fig. 2(b), is shown in Fig. 2(f). The strong dip in the center of the profile could indicate Landau branching^{18,31,32}, as sketched in the inset in Fig. 2(f). The absence of a superconducting region (*i.e.* zero field because of complete screening) in the center of the *volcano* is attributed to the masking effects due to the spreading of the magnetic field and the finite size of the SQUID. Another scenario would be the presence of a superconducting tube inside the normal tube, as predicted for the high field limit in the model of Clem *et al.*³³, where superconducting tubes are surrounded by normal regions. We can not distinguish between the two scenarios.

The closed topology structures and their arrangement have been modeled in the past by a number of theo-

reticians^{33,34}, exploring the minimal energy state with the domain wall energy and field energy contributing to the total energy. They could predict the transition from tubular to laminar shapes of flux structures, their size and density as a function of the applied magnetic field and the thermodynamic critical field. Clem *et al.* proposed a coherent description from the low field region, describing normal tubes in the superconducting state, followed by intermediate fields, with laminar structures of alternating normal and superconducting regions, up to superconducting tubes surrounded by normal state regions close to the critical field.

We first determine the domain wall width, δ , based on either Refs.^{31,34} or³³. A first way to calculate δ as a function of the reduced field, $h = H_a/H_c$, and the sample thickness, d , is from the flux spot diameter D via the relation $\delta = D^2(1 - h)(1 - \sqrt{h})/(2d)$, or from the lattice parameter between adjacent flux spots, a , via the relation $\delta = a^2h(1 - h)(1 - \sqrt{h})/(2d)$. Choosing Fig. 2(b) to measure the lattice parameter and sizes of spots ($D = 13 \pm 2 \mu\text{m}$ and $a = 22.7 \pm 2.5 \mu\text{m}$), we obtain a domain wall width of $0.25 \pm 0.08 \mu\text{m}$ based on the spot size and $0.25 \pm 0.06 \mu\text{m}$ based on the lattice parameter, respectively for the gives case ($h = 3/9.14$ and $d = 97 \mu\text{m}$). A second way to calculate δ is given by Clem *et al.*, who add in their expression for δ as a parameter the normalized free energy, Φ_1 , that attains the value $\Phi_1 = 0.079$ for this field. Based on the spot size diameter, the domain wall width can be calculated from the rela-

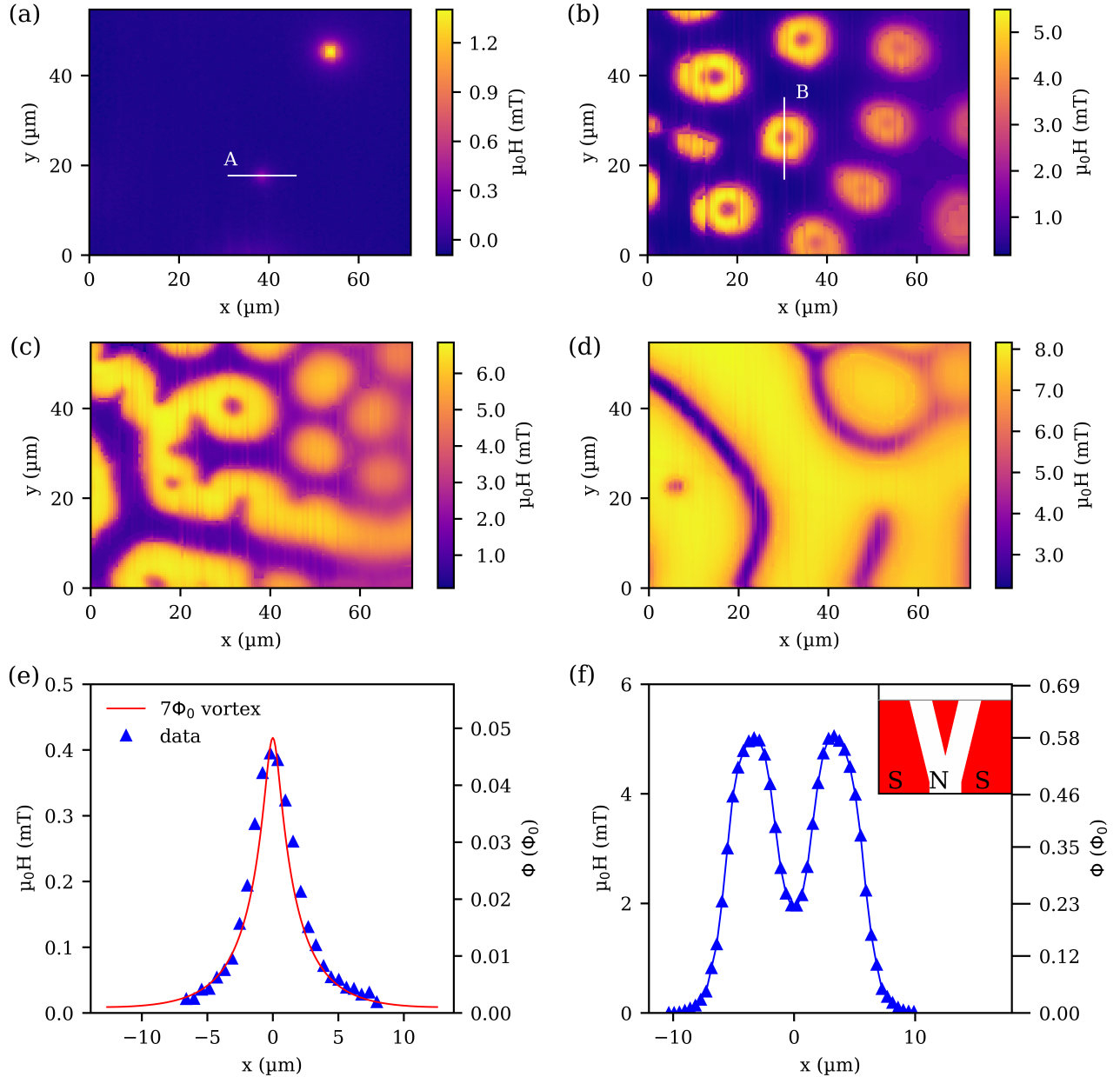


FIG. 2: (Color online) Panels (a) to (d): ZFC scanning SQUID images taken at a temperature of 900 mK at an applied field of 1 mT, 3 mT, 4.5 mT and 7.5 mT, respectively (all images from the same cool down). Panels (e) and (f): Field profiles along the lines A and B as shown in (a) and (b), respectively. As comparison, the theoretical field distribution of a $7\Phi_0$ -vortex with $\lambda = 2.1 \mu\text{m}$ scanned at 350 nm is represented in red in (e). The inset in (f) represents the schematics of flux tube branching at the surface of the sample.

tion $\delta = (D\Phi_1/h)^2/d$ and we obtain $\delta = 0.10 \pm 0.06 \mu\text{m}$. Alternatively, Clem *et al.* estimate δ from a normalized lattice parameter $R_0 = (\sqrt{3}/2\pi)^{1/2}a = 11.9 \mu\text{m}$ with help of the relation $\delta = (2R_0\Phi_1)^2/(dh)$. This results in $\delta = 0.11 \pm 0.03 \mu\text{m}$. Since the model of Clem *et al.* does not take into account the spreading of the flux tubes near the surface and the presence of the flux minima that

we observe, we argue the most reliable estimates of the domain wall width are the ones based on the lattice parameter, thus $\delta = 0.11 \pm 0.03 \mu\text{m}$ according to the model of Clem *et al.* or $0.25 \pm 0.08 \mu\text{m}$ according to the model of Goren *et al.*

Above a certain threshold field, H_f , the single round magnetic structures fuse into laminar domains, as for instance shown by the scan taken at 4.5 mT reported in

Fig. 2(c). The values $H_f(T)$ in Fig. 1(b) show a relatively high dispersion which we attribute to the coexistence and competing effects of structures with a closed (tubular) topology and an open (laminar) topology. Such coexistence of shapes has been reported in the literature before, and a quantitative analysis has been made in several model cases^{31,34-36}. This coexistence is in agreement with the small free energy difference between the flux arrangements³³.

The domain wall width is in all configurations an important parameter. Based on Ref.³³ we have determined also the domain wall width in the laminar state observed at 4.5 mT (Fig. 2(c)). The distance between two normal laminae is $2R_0 = 20 \mu\text{m}$ and the width of the intermediate state laminae is $2R = 8 \mu\text{m}$. The normalized free energy at the reduced field $h = 4.5/9.14$ is $\Phi_2 = 0.092$. The domain wall width derived from the period of the normal laminae is expressed as $\delta = (4R_0\Phi_2)^2/d$, and we obtain $\delta = 0.14 \mu\text{m}$. On the other hand, the domain wall width derived from the width of the normal laminae is expressed as $\delta = (4R\Phi_2/h)^2/d$, which leads to a value $\delta = 0.09 \mu\text{m}$.

It is remarkable that the model of Clem *et al.* gives consistent results for δ considering the level of abstractness of the model compared to the complex shapes observed in real samples.

As the field increases, the laminae become wider and occasional some tubular regions are observed, for instance at $x = 5 \mu\text{m}$, $y = 22 \mu\text{m}$ in the scans of Fig. 2(d). This tells us that the high field equilibrium state in our case is a mixture of tubular and laminar superconducting structures (see Fig. 2(d)) at odds with exclusively tubular structures predicted for the high field phase in the Clem *et al.* model.

Branching of normal domains at low and intermediate fields could be peculiar because we observe only one single funnel-like branch per normal domain. In contrast, in many other intermediate state superconductors more complex branching patterns have been observed^{31,37}. Branching can even produce isolated superconducting islands (inclusions). A priori, these closed topology structures should obey flux quantization³⁸, and the appearance of isolated single- Φ_0 structures, such as reported in Refs.^{7,15}, cannot be excluded. Finally, we remark that branching is expected to occur only for a sample thickness larger than the critical thickness $d_s \approx 800 \times \delta$ ³¹. With our estimate of the domain wall width in the range 0.1 to $0.25 \mu\text{m}$, d_s falls in the range $80 - 200 \mu\text{m}$, while the sample thickness is $97 \mu\text{m}$. Thus observation of branching is in favor of a domain wall width of the order of $0.12 \mu\text{m}$. The absence of a more intricate branching pattern may be explained by the fact that the sample thickness is at the limit of the branching criteria.

The partial duplication of the structure at $x=15 \mu\text{m}$ in Fig. 2(b) denotes movement of the structures, which we attribute to the coupling between the SQUID's magnetic field and the structure itself. This movement can only be observed in case of weak pinning. This effect can also be

deduced from the vertical lines in Fig. 2(b)-(d).

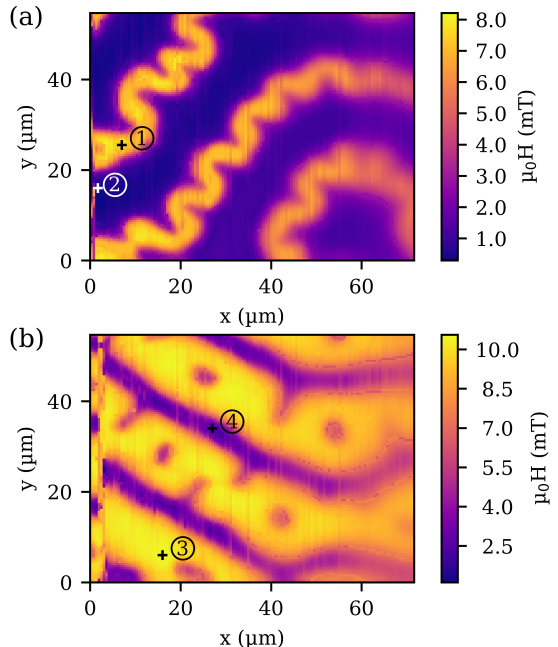


FIG. 3: (Color online) FC images at 300 mK: 3.5 mT in (a) and 8 mT in (b). Points 1 to 4 indicate the maximal and minimal measured fields of each scan referred to in Fig. 4.

B. PdTe₂ Field Cooled

Above we have investigated flux structures in the intermediate phase after ZFC. Alternatively, one can reach the intermediate state by field cooling (FC) from the normal phase. Since the obtained magnetic structures sensitively depend on the domain wall energy, the magnetic-field energy and pinning forces, the intermediate state patterns can be very different^{31,34,37}. In the FC case, the expulsion of the flux in general results in laminar structures, that connect to the edges of the crystal. Two examples of such open topology structures are presented in Fig. 3, scanned at 0.3 K in 3.5 mT and 8 mT applied fields. The 8 mT scan shows a mixture of laminar and tubular superconducting structures, while in the 3.5 mT scan meandering normal state laminae are present.

IV. DISCUSSION

One of the major results from the present SSM measurements is the direct observation of the intermediate phase on a local scale in the field range $(1 - N)H_c < H_a < H_c$. According to theory the magnetic field in the normal domains should always be equal to H_c ¹⁸. In the case of PdTe₂ this was demonstrated by μSR measurements that probe the field in the bulk of the normal

domains in the crystal¹⁹. However, the field at the surface probed in our SSM experiment can be considerably smaller.

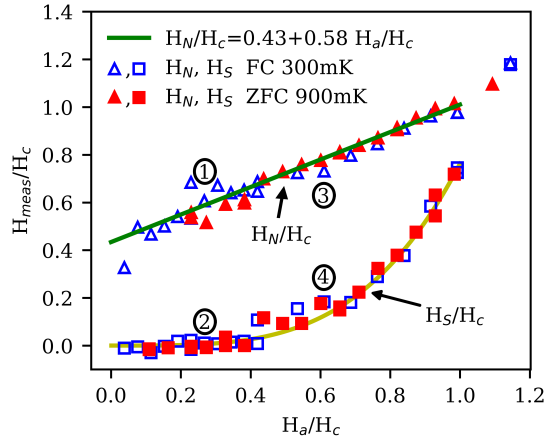


FIG. 4: (Color online) The normal-state field, H_N (triangles), and the superconducting-state field, H_S (squares), as a function of the applied field, H_a , for, in red/full, ZFC (900 mK) and, in blue/empty, FC (300 mK) measurements. The green (dark gray) line represents the linear fit: $H_N/H_c = 0.43 + 0.58 H_a/H_c$. The yellow (light gray) line is a guide to the eye. Points 1 to 4 are references to the corresponding points in the images of Fig. 3.

This is shown in Fig. 4 where we trace H_N , the maximal field of the normal state structure, normalized by H_c , as a function of the reduced applied field H_a/H_c . In the bulk case, $H_N/H_c = 1$ is verified¹⁹, but we observe that H_N is a linear function of the applied field. A possible explanation is a spreading of the magnetic field near the surface. We try to use conservation of flux to estimate the degree of spreading necessary to explain our measurement of the magnetic field at the sample surface. Taking into account conservation of flux in a single tubular normal domain, $\Phi = \mu_0 H_c S_{bulk} \approx \mu_0 H_{surf} S_{surf}$, where S_{bulk} and S_{surf} are the cross sections of the flux tube in the bulk and at the surface respectively. This implies the ratio H_{surf}/H_c behaves as S_{bulk}/S_{surf} . We can consider $H_N = H_{surf}$ as a first approximation and $H_{surf}/H_c \approx 0.5$ at the onset of the intermediate phase (see Fig. 4), which implies the diameter d_{surf} of a flux tube near the surface would be 1.4 times the one in the bulk d_{bulk} . By increasing the field this effect becomes smaller and smaller, as the normal state is approached, and the energy difference vanishes. The magnetic field above the superconducting regions (H_S) increases steeply upon increase of the applied field, which we attribute to the increase of the stray field emanating from the normal regions. In general, measuring the magnetic field at the surface of a multi domain material is an intricate prob-

lem³⁹. Surface μ SR experiments in which the muons are implanted near the surface could shed more light on this problem⁴⁰.

Our visualization of the evolution of the magnetic flux structure as a function of the applied field shows a change from closed to open topological patterns at a field H_f (see Fig. 1(b)). The equilibrium topology can be described using overall energy minimization of the wall-energy and field-energy terms^{33,41}. The competition of these two terms can be studied from scans like those in Figs 2 and 3. A way to quantify the change from a tubular pattern to a laminar pattern is to measure the intermediate state (IS) area, s , and the normal-superconducting (N-S) interface perimeter, p , of different domains at the surface. Their ratio p/s and p^2/s will change at the transition from the tubular to the laminar pattern. The perimeter term is related to the wall energy and the surface term is related to the field energy.

We analyzed the perimeter and the surface of up to ~ 10 closed and open topologies for a given field and field history. Given the asymmetry of the distribution of the ratios p/s and p^2/s in the ZFC measurements, we choose to trace the lower bound, which shows clear tendencies. In this case (see Fig. 2(b)), we have a closed topology pattern, *i.e.* tubes, therefore we expect the perimeter over surface ratio to follow $p/s = 2/r$ and $p^2/s = 4\pi$. As tubular structures prevail for fields lower than H_f , the ratio p^2/s is constant at a value of $\sim 12.9 \approx 4\pi$ (see Fig. 5). Above this field, tubular structures and laminae coexist, thus the ratio p^2/s presents two components, one constant due to the tubular structures and another one, due to the laminae, that tends to zero as the normal state surface area increases faster than the perimeter. For the same measurements, the ratio p/s behaves as $\alpha + \beta/H_a$ for the entire studied range (see Fig. 5). We undertook the same analysis for the data obtained during FC measurements. The ratios p/s and p^2/s tend to go to zero as the applied field approaches $\mu_0 H_c$, but a clear tendency could not be revealed.

These observations have allowed us to estimate the appearance of laminae at a reduced applied field $h = 0.55$ and we find that the perimeter over surface ratio seems to depend on the applied field as $1/H_a$, up to the critical field. This ratio does not distinguish between laminar or tubular patterns.

V. SUMMARY AND CONCLUSION

Using a high resolution scanning μ -SQUID microscope we have investigated the local magnetic flux structure in the superconducting phase of PdTe₂ when exposed to a magnetic field. The data have been taken on a thin single crystal with a demagnetization factor $N = 0.82$. We confirmed the superconducting phase diagram with intermediate phase by measuring the local magnetization during field sweeps. This is indicative of a very low resistance to flux penetration and weak flux pinning in PdTe₂.

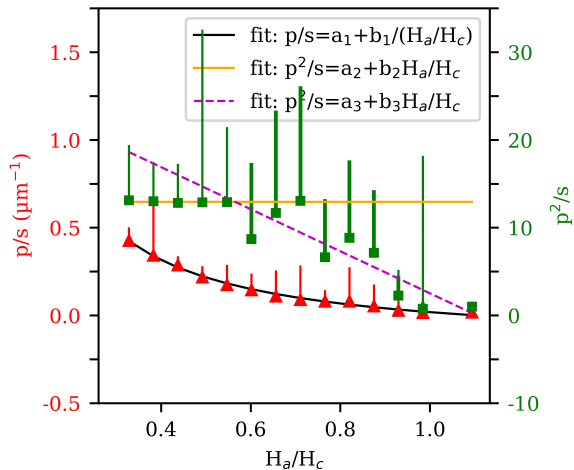


FIG. 5: (Color online) Perimeter over surface ratio, p/s , and perimeter squared over surface ratio, p^2/s , of the intermediate state pattern derived from images at different applied magnetic fields acquired after ZFC. yellow line (light gray): $p^2/s = 0.11 H_a/H_c + 12.9$ (presence of tubular pattern), magenta line (dashed) (appearance of laminar structures), and blue (dark gray) line $p/s = 0.2 H_c/H_a - 0.185$.

The scanned images reveal the intermediate state and thus type-I superconductivity. By analyzing the SQUID signal as a function of the field at several fixed temperatures we have determined $(1 - N)H_c$ and H_c and constructed the ZFC phase diagram. The measured value $H_c = 13.6$ mT is in excellent agreement with the literature¹⁷. In the intermediate phase we also identify a field H_f where tubular, closed topology flux structures fuse into laminar, open topology structures. Both structures exist at the same time in fields above H_f .

The stability of the structures is supported by the competition of surface and volume energies, which we could analyze from measurements of the perimeter and surface ratios. The smallest magnetic flux structure we observed is comparable to that of a $7\Phi_0$ vortex. Furthermore, we observed branching, typical for the intermediate state, and magnetic field spreading at the surface. Also the field measured at the surface of the normal domains is smaller than H_c , and shows a linear increase upon increasing applied field. This suggests a difference between the cross section of the flux tube in the bulk, S_{bulk} , and at the surface, S_{surf} .

We estimated the domain wall width in analyzing the size and the period of the flux structures using the model of Goren and Tinkham³⁴ and the model of Clem *et al.*³³. The estimated values place our sample thickness at the limit for Landau branching. Tubular superconducting regions persist up to the highest fields, they coexist with laminar superconducting structures.

Finally, single-quantum vortices and type-II superconducting regions were not detected in our experiment, which excludes type II/1 behavior or a mixture of type-I and type-II behavior. The scanning SQUID data fully support PdTe₂ is a type-I superconductor.

VI. ACKNOWLEDGEMENTS

PGC acknowledges funding from the Innovation Programme under the Marie Skłodowska-Curie grant agreement No. 754303 and the *Fondation des Nanosciences* (FCSN 2018 02D). The research leading to these results received funding from the European Unions Horizon 2020 Research and Innovation Programme, under Grant Agreement No. 824109, the European Microkelvin Platform (EMP).

* pablo.garcia-campos@neel.cnrs.fr

† Klaus.Hasselbach@neel.cnrs.fr

¹ X.-L. Qi and S.-C. Zhang, *Rev. Mod. Phys.* **83**, 1057 (2011).

² S. D. Sarma, M. Freedman, and C. Nayak, *npj Quantum Information* **1**, 15001 (2015).

³ Y. Ando and L. Fu, *Annu. Rev. Condens. Matter Phys.* **6**, 361 (2015).

⁴ M. Sato and S. Fujimoto, *J. Phys. Soc. Jpn* **85**, 027001 (2016).

⁵ M. Sato and Y. Ando, *Rep. Progr. Phys.* **80**, 076501 (2017).

⁶ Y. Liu, J.-Z. Zhao, L. Yu, C.-T. Lin, A.-J. Liang, C. Hu, Y. Ding, Y. Xu, S.-L. He, L. Zhao, et al., *Chinese Phys. Lett.* **32**, 067303 (2015).

⁷ O. J. Clark, M. J. Neat, K. Okawa, L. Bawden, I. Marković, F. Mazzola, J. Feng, V. Sunko, J. M. Riley, W. Meevasana, et al., *Phys. Rev. Lett.* **120**, 156401 (2018).

⁸ M. S. Bahramy, O. J. Clark, B.-J. Yang, J. Feng, L. Bawden, J. M. Riley, I. Markovic, F. Mazzola, V. Sunko, D. Biswas, et al., *Nature Mat.* **17**, 21 (2018).

⁹ A. A. Soluyanov, D. Gresch, Z. Wang, Q. Wu, M. Troyer, X. Dai, and B. Bernevig, *Nature* **257**, 495 (2015).

¹⁰ J. Guggenheim, F. Hulliger, and J. Müller, *Helvetica Physica Acta* **34**, 408 (1961).

¹¹ Amit and Y. Singh, *Phys. Rev. B* **97**, 054515 (2018).

¹² M. V. Salis, P. Rodire, H. Leng, Y. K. Huang, and A. de Visser, *J. Phys.: Condens. Matter* **30**, 505602 (2018).

¹³ S. Teknowijoyo, N. H. Jo, M. S. Scheurer, M. A. Tanatar, K. Cho, S. L. Bud'ko, P. P. Orth, P. C. Canfield, and R. Prozorov, *Phys. Rev. B* **98**, 024508 (2018).

¹⁴ S. Das, Amit, A. Sirohi, L. Yadav, S. Gayen, Y. Singh, and G. Sheet, *Phys. Rev. B* **97**, 014523 (2018).

¹⁵ A. Sirohi, S. Das, P. Adhikary, R. R. Chowdhury, A. Vashist, Y. Singh, S. Gayen, T. Das, and G. Sheet, *J. Phys.: Condens. Matter* **31**, 085701 (2019).

- ¹⁶ T. Le, L. Yin, Z. Feng, Q. Huang, L. Che, J. Li, Y. Shi, and X. Lu, Phys. Rev. B **99**, 180504 (2019).
- ¹⁷ H. Leng, C. Paulsen, Y. K. Huang, and A. de Visser, Phys. Rev. B **96** (2017).
- ¹⁸ M. Tinkham, *Introduction to Superconductivity* (Dover Publications, Mineola, New York, 2004).
- ¹⁹ H. Leng, J.-C. Orain, A. Amato, Y. Huang, and A. de Visser, Phys. Rev. B **100**, 224501 (2019).
- ²⁰ H.-J. Noh, J. Jeong, E.-J. Cho, K. Kim, B. I. Min, and B.-G. Park, Phys. Rev. Lett. **119**, 016401 (2017).
- ²¹ H. Leng, A. Ohmura, L. N. Anh, F. Ishikawa, T. Naka, Y. K. Huang, and A. de Visser, J. Phys.: Condens. Matter **32**, 025603 (2020).
- ²² F. Fei, X. Bo, R. Wang, B. Wu, J. Jiang, D. Fu, M. Gao, H. Zheng, Y. Chen, X. Wang, et al., Phys. Rev. B **96**, 041201 (2017).
- ²³ N. Kimura, N. Kabeya, K. Saitoh, K. Satoh, H. Ogi, K. Ohsaki, and H. Aoki, J. Phys. Soc. Jpn **85**, 024715 (2016).
- ²⁴ Y. Wang, R. Lortz, Y. Paderno, V. Filippov, S. Abe, U. Tutsch, and A. Junod, Phys. Rev. B **72**, 024548 (2005).
- ²⁵ D. J. Hykel, Z. S. Wang, P. Castellazzi, T. Crozes, G. Shaw, K. Schuster, and K. Hasselbach, J. Low Temp. Phys. **175**, 861 (2014).
- ²⁶ C. Veauvy and K. Hasselbach, Rev. Sci. Instr. **73**, 3825 (2002).
- ²⁷ L. Thomassen, Z. Phys. Chem. **B2**, 349 (1929).
- ²⁸ E. Pardo, D.-X. Chen, and A. Sanchez, J. Appl. Phys. **96**, 5365 (2004).
- ²⁹ E. Pardo, D.-X. Chen, and A. Sanchez, IEEE Trans. Magn. **40**, 1491 (2004).
- ³⁰ J. R. Kirtley, V. G. Kogan, J. R. Clem, and K. A. Moler, Phys. Rev. B **59**, 4343 (1999).
- ³¹ R. P. Huebener, *Magnetic Flux Structures in Superconductors* (Springer-Verlag, Berlin, 1979).
- ³² L. D. Landau, Zh. Eksp. Teor. Fiz. **7**, 371 (1937).
- ³³ J. R. Clem, R. Prozorov, and R. J. Wijngaarden, Phys. Rev. B **88**, 104504 (2013).
- ³⁴ R. N. Goren and M. Tinkham, J. Low Temp. Phys. **5**, 465 (1971).
- ³⁵ E. H. Brandt and M. P. Das, J. Supercond. Nov. Magn. **24**, 57 (2011).
- ³⁶ G. R. Berdiyrov, A. D. Hernandez, and F. M. Peeters, Phys. Rev. Lett. **103**, 267002 (2009).
- ³⁷ R. Prozorov, R. W. Giannetta, A. A. Polyanskii, and G. K. Perkins, Phys. Rev. B **72**, 212508 (2005).
- ³⁸ J. Ge, J. Gutierrez, J. Cuppens, and V. V. Moshchalkov, Physica C **503**, 38 (2014).
- ³⁹ V. Kozhevnikov, R. J. Wijngaarden, J. de Wit, and C. Van Haesendonck, Phys. Rev. B **89**, 100503 (2014).
- ⁴⁰ V. Kozhevnikov, A. Suter, T. Prokscha, and C. V. Haesendonck (2018), 1802.08299.
- ⁴¹ L. Landau, J. Phys. U.S.S.R. **7** (1943).